journal

Spinel Compounds: Structure and Property Relations

J. Am. Ceram. Soc., **82** [12] 3321–29 (1999)

Comparison of Ion-Beam Irradiation Effects in X_2YO_4 Compounds

LuMin Wang,*,† WeiLang Gong,‡ ShiXin Wang,† and Rodney C. Ewing*,†

Department of Nuclear Engineering and Radiological Sciences, University of Michigan, Ann Arbor, Michigan 48109-2104; and
Center for Radioactive Waste Management, University of New Mexico, Albuquerque, New Mexico 87131

The effects of 1.5 MeV Kr-ion irradiation on seven X_2YO_4 phases with the olivine ($A_2^{VI}B^{IV}O_4$), spinel ($A^{IV}B_2^{VI}O_4$), and phenakite structures have been investigated using *in situ* and high-resolution transmission electron microscopy (HRTEM) over a wide temperature range (20–873 K). At low temperatures (<200 K), the olivine and phenakite are susceptible to radiation-induced amorphization with a critical amorphization dose of 0.2–0.5 displacement per atom (dpa). The critical amorphization dose increases with increasing irradiation temperature at varying rates for the various phases, resulting in a distinct critical amorphization temperature for each phase. For the Mg-Fe series of olivine, the susceptibility to amorphization at higher temperatures (room temperature or above) increases with increasing Fe content. Although the spinel phases are, in general, much more resistant to amorphization, a high-pressure metastable spinel phase, γ-$SiFe_2O_4$, is easily amorphized at doses <0.2 dpa at temperatures below 723 K. This phase decomposes after irradiation at 873 K. At 20 K, complete amorphization of the $FeCr_2O_4$ spinel (chromite) is achieved at ~4 dpa, but no evidence of amorphization is observed in $MgAl_2O_4$ spinel after 5.4 dpa. The distinct differences in the relative susceptibility of these phases to amorphization are discussed in terms of the structural and chemical controls on the amorphization process.

I. Introduction

THE X_2YO_4 system is characterized by a rich variety of compositions (e.g., X = Mg, Fe, Mn, Ca, Ni, Co, Zn, Be, Li, Al, Cr, and rare-earth elements; Y = Si, Ge, Be, As, B, and P); extensive solid solutions between pure, end-member compositions; and a variety of structure types (e.g., the hexagonal-close-packed (hcp) derivative olivines ($A_2^{VI}B^{IV}O_4$), the cubic-close-packed (ccp) spinels ($A^{IV}B_2^{VI}O_4$), and the hexagonal phenakite structure). Because these materials usually have only two unique cations, they are also the simplest among the multication "complex" ceramics. Thus, they form an ideal group for investigating the structural and bonding control on radiation-induced amorphization of complex ceramic materials.

The temperature dependence of the critical amorphization dose, D_c, for seven X_2YO_4 compositions has been investigated by *in situ* transmission electron microscopy (TEM) during ion-beam irradiation in this comparative study. These phases include forsterite (Mg_2SiO_4), fayalite (α-Fe_2SiO_4), phenakite (Be_2SiO_4), synthetic Mg_2GeO_4, spinel ($MgAl_2O_4$), chromite ($FeCr_2O_4$), and γ-$SiFe_2O_4$ (a spinel phase formed under high pressure). Among these phases, Mg_2SiO_4, γ-Fe_2SiO_4, and Mg_2GeO_4 have the olivine structure, and Mg_2SiO_4 and γ-Fe_2SiO_4 are the end members of a complete solid-solution $(Mg,Fe)_2SiO_4$ composition series (several intermediate compositions of this series also have been studied). $MgAl_2O_4$, $FeCr_2O_4$, and γ-$SiFe_2O_4$ have the spinel structure. $MgAl_2O_4$ spinel has been reported to be very resistant to irradiation-induced damage and amorphization,[1,2] and has been the subject of numerous radiation damage studies.[3–7]

The olivine structure-type consists of a slightly distorted hcp array of oxygen anions with one-half of the octahedral sites occupied by A-site cations (e.g., Mg and Fe) and only one-eighth of the tetrahedral sites occupied by B-site cations (e.g., Si or Ge). The polyhedral structure of olivine is illustrated in Fig. 1. The important structural features of the olivine structure are the "serrated chains," parallel to the *c*-axis, of two symmetrically independent, edge-sharing octahedra, $M(1)O_6$ and $M(2)O_6$. The M(1) octahedron shares six of its 12 edges with other polyhedra (two with $M(1)O_6$, two with $M(2)O_6$, and two with tetrahedra), and the M(2) octahedron shares only three edges (two with $M(1)O_6$ and one with a tetrahedron). The SiO_4 tetrahedral monomers are isolated from one another, but are joined along three edges and one apex to the edge-sharing octrahedral chains. Significant structural distortion occurs in the olivine structure-type; e.g., the space group symmetry of the hcp array of anions decreases from $P6_3/mcc$ (ideal hcp olivine structure) to *Pbnm* (actual olivine structure). In the $(Mg,Fe)_2SiO_4$ olivines, Mg and Fe^{2+} occupy the M1 and M2 sites without specific preference for either site. The unit cell of

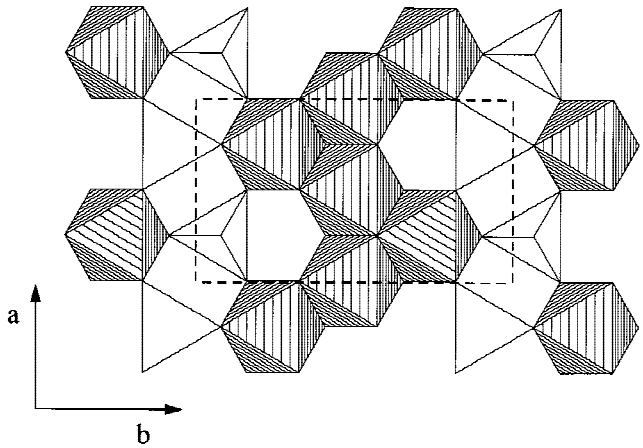

Fig. 1. Polyhedral structure illustraton of olivine, looking down the [001] axis (with only the occupied polyhedra shown). Si or Ge atoms occupy the tetrahedral sites. Mg, Fe^{2+}, and other sixfold coordinated cations occupy the octahedral sites. Oxygen atoms are at the corners of polyhedra. Dashed lines indicate the size of a unit cell.

K. E. Sickafus—contributing editor

Manuscript No. 189659. Received December 28, 1998; approved September 21, 1999.

Supported by the Office of Basic Energy Sciences, U.S. Department of Energy, under Grant No. DE-FG02-97ER45656.

Presented at the 100th Annual Meeting of The American Ceramic Society, Cincinnati, OH, May 6, 1998 (Basic Science Division Special Session on Spinel Compounds: Structure and Property Relations, Paper No, BS13-020-98).

*Member, American Ceramic Society.
†University of Michigan.
‡University of New Mexico.

olivine is orthorhombic, and the lattice parameters increase with increasing Fe^{2+} content; i.e., $a_0 = 0.475$, $b_0 = 1.020$, and $c_0 = 0.598$ nm for forsterite, and $a_0 = 0.482$, $b_0 = 1.048$, and $c_0 = 0.609$ nm for fayalite. In Mg_2GeO_4, Ge substitutes for Si in tetrahedral sites, but the increased covalency of the Ge–O bond leads to lengthening of the shared edges.

Compositions in the $(Mg,Fe)_2SiO_4$ binary system, with the end members forsterite (Mg_2SiO_4) and fayalite (Fe_2SiO_4), are common rock-forming orthosilicate minerals. The melting temperature for the Mg-rich end member (1700°C) of the series is substantially higher than that of the Fe^{2+}-rich end member (1205°C).

The spinel structure (*Fd*3*m*; $Z = 8$), with the general formula of γ-$A^{IV}B_2^{VI}O_4$ (normal spinel), is a face-centered ccp structure-type in which one-eighth of the tetrahedral sites and one-half of the octahedral sites are occupied by A- and B-site cations, respectively. The nearly perfect ccp stacking array of the oxygens occurs along the [111]. The occupied octahedra are joined along edges to form rows and planes parallel to {111} of the structure, and the occupied tetrahedra provide cross links between layers of octahedra. The polyhedral structure of spinel is illustrated in Fig. 2. Many compounds that crystallize in the spinel structure have important technological applications, including use as magnetic materials and high-temperature ceramics for applications in a radiation environment. Moreover, silicate spinels are important phases in the earth's mantle.[8,9] Consequently, the physical and chemical properties of spinels are of general interest in fields ranging from materials physics to geophysics.

The olivine and spinel phases are related because they have similar chemical stoichiometry and because the olivine–spinel transition occurs under high pressure. For example, fayalite (α-Fe_2SiO_4) transforms to spinel (γ-$SiFe_2O_4$) at ~5.6 GPa and at 1000°C.[10] The olivine–spinel transition first results in the formation of an intermediate phase, modified spinel phase.[11,12] The relative stability of the olivine and spinel forms of $(Mg,Fe)_2SiO_4$ has been studied extensively.[13,14]

Phenakite (Be_2SiO_4) has a hexagonal structure in which both of the A- and B-site cations are in tetrahedral coordination. The SiO_4 tetrahedron shares each of its four corners with two BeO_4 tetrahedra, and the BeO_4 tetrahedra share each of their corners with one SiO_4 and one BeO_4 tetrahedron. Four- and six-membered rings of tetrahedra alternate in the (001) plane, whereas three-membered rings of tetrahedra are found perpendicular to the (001). The structure also can be visualized in terms of its distinctive chains of tetrahedra parallel to the *c*-axis with the regular pattern Be-Be-Si-Be-Be-Si-. The polyhedral structure of phenakite is illustrated in Fig. 3. The phenakite structure has a "stiff" atomic arrangement, and no significant deformation of the structure is possible because of the topological connections between the tetrahedra.[15] Interpolyhedral ⟨O–O⟩ distances in most inorganic crystal structures have ⟨O–O⟩ distances ≥0.290 nm. For example, the ⟨O–O⟩ distance is >0.333 nm for quartz and 0.290 nm for kyanite. However, the shortest interpolyhedral ⟨O–O⟩ distance found in a silicate occurs in phenakite (0.275 nm). This suggests that phenakite has an exceptionally high bond strength between these polyhedra. The uniquely strong bonding of these polyhedra makes phenakite a good phase for studying the role of bond strength on the susceptibility to radiation-induced amorphization.

II. Experimental Procedures

Fayalite (Fe_2SiO_4), phenakite (Be_2SiO_4), Mg_2GeO_4, and $MgAl_2O_4$ are synthetic end-member compositions. Forsterite (Mg_2SiO_4) and chromite ($FeCr_2O_4$) are natural phases, and they have actual compositions of $(Mg_{0.88}Fe_{0.12})_2SiO_4$ and $(Fe_{0.6}Mg_{0.4})(Cr_{0.7}Al_{0.3})_2O_4$, as determined by analytical electron microscopy. The high-pressure polymorph of Fe_2SiO_4—γ-$SiFe_2O_4$—has been synthesized at 7.0 GPa and 1473 K using a 2000-ton uniaxial split-sphere apparatus at the Geophysical Laboratory, Carnegie Institution, Washington, D.C. The spinel structure of the phase has been confirmed by optical and micro-Raman spectroscopic techniques.

The TEM samples prepared by Ar-ion milling were irradiated with 1.5 MeV Kr^+ ions in the HVEM-Tandem Facility at Argonne National Laboratory[16] at a dose rate of 3.4×10^{15} ions/(m^2·s). The dose rate for irradiating $MgAl_2O_4$ and $FeCr_2O_4$ was increased to 3.4×10^{16} ions/(m^2·s) after realizing that higher doses were required to cause an effect in these materials. The HVEM-Tandem Facility consists of a high-voltage electron microscope (HVEM) connected to a tandem ion accelerator; thus, the selected area electron diffraction (SAED) pattern and TEM image can be monitored *in situ* during ion irradiations. The HVEM was used at an accelerating

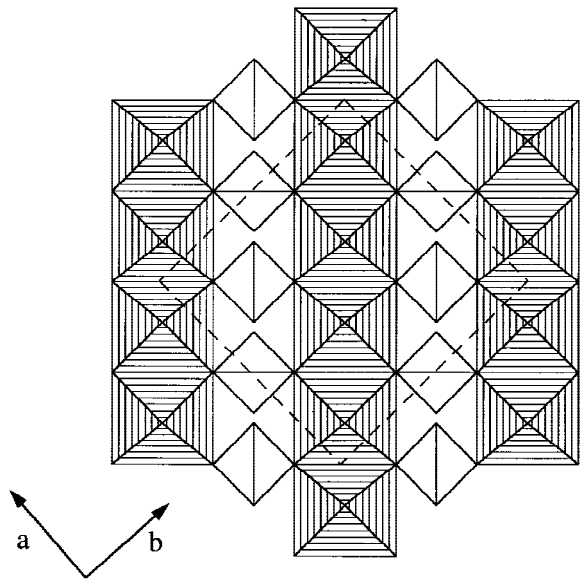

Fig. 2. Polyhedral structure illustration of spinel, looking down the [001] axis (with only the occupied polyhedra shown). Mg or other four-coordinated A-site cations are usually in the tetrahedral sites. Al and other six-coordinated B-site cations are in the octahedral sites. Oxygen atoms are at the corners of polyhedra. Dashed lines indicate the size of a unit cell.

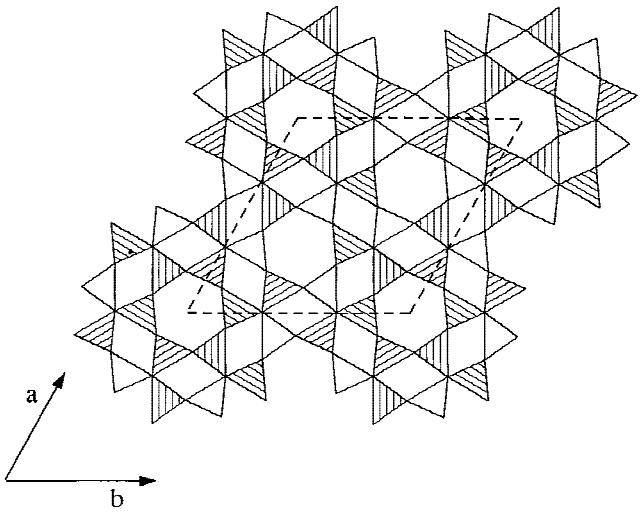

Fig. 3. Polyhedral structure illustration of phenakite looking down the [001] axis (with only the occupied polyhedra shown). Phenakite has a hexagonal structure in which both A-site (Be) and B-site (Si) cations are in tetrahedral coordination. SiO_4 tetrahedron shares each of its four corners with two BeO_4 tetrahedra, and BeO_4 tetrahedra (shaded) share each of their corners with one SiO_4 and one BeO_4 tetrahedron. Dashed lines indicate the size of a unit cell.

voltage of 300 keV. The SAED was monitored at the maximum sample thickness where a clear diffraction pattern could be obtained, because thinner regions become amorphous at lower doses because of surface effects. The irradiations were performed between 20 to 723 K, using a liquid-helium-cooled cold stage or a hot stage. The maximum temperature increase due to beam heating was 60°C. Most of the 1.5 Kr^+ ions completely penetrated the electron-transparent thickness (~300 nm) of the samples, and the Kr^+ concentration introduced into the sample was negligible. Because of differences in the density and displacement energy of the different targets, the per-ion energy loss and damage production in the observable sample thickness were different. TRIM[17] calculations were performed to convert the critical ion fluence to a damage dose in displacements per atom (dpa). However, this conversion may not have been accurate, because a displacement energy (E_d) of 25 eV was assumed for most of the materials whose E_d was not known. A value of 40 eV was used for $MgAl_2O_4$[3] and $FeCr_2O_4$ spinels. Although the real values of E_d for these phases may have been off by a factor of 2, the errors introduced using an assumed E_d were not significant, as compared with the large differences in the critical amorphization doses, especially at elevated temperatures. The effects of variations in the densities of the materials on displacement efficiency have been accounted for by the TRIM calculation. A more-detailed discussion on this experimental method has been presented in Ref. 18.

Before and after ion irradiation, the samples were also examined by high-resolution TEM (HRTEM; Model 2000FX or Model 2010 electron microscope, JEM) at the University of New Mexico, which was operated at 200 kV. The final ion milling was completed using low-energy Ar ions (3–3.5 kV) at low angles (<11°), and no significant amorphization was observed after the ion milling.

III. Results

Most of the phases were amorphized by the 1.5 MeV Kr^+ ions at low temperatures. A typical series of SAED patterns obtained during the *in situ* observation of the ion-beam-induced crystalline-to-amorphous transformation is shown in Fig. 4 (the series is obtained from 1.5 MeV Kr^+-irradiated forsterite at 300 K).

Before irradiation, a single-crystal diffraction pattern was obtained (Fig. 4(A)). The progressive amorphization process with the increasing ion dose was evidenced by the gradual fading of Bragg-diffraction maxima intensities and the appearance of an amorphous diffraction halo (Figs. 4(B) and (C)). This change in SAED pattern was accompanied by the loss of diffraction contrast (bend contours and thickness fringes) in the bright-field image. Amorphization was considered complete when all the Bragg-diffraction maxima completely disappeared in the diffraction pattern (Fig. 4(D)) after a critical amorphization dose, D_c.

This type of SAED series is the same as those obtained from self-damaged actinide-containing minerals that have received various α-decay doses due to different actinide content and mineral age.[19,20] Not all the diffraction spots fade and disappear at the same time. For example, the diffraction spots indicated by arrows in Fig. 4(A) (diffractions from the cation sublattice) fade and disappear much earlier than the other spots (diffractions from the anion sublattice), indicating that cation disordering has occurred prior to amorphization.

The progessive amorphization process in forsterite was also apparent in the HRTEM images taken before and after various ion doses, as shown in Fig. 5. Before irradiation, a near-perfect lattice image was obtained, as shown in Fig. 5(A). At low ion doses, isolated amorphous domains were observed in the crystalline matrix (Fig. 5(B)). With increased ion dose, the amorphous domains increased in number and overlapped; thus, only isolated crystallites were observed in the amorphous matrix, as in Fig. 5(C). The observation of nanometer-scale, discrete amorphous domains confirmed the heterogeneous nature of the amorphization process and suggested that amorphization had occurred by direct cascade quenching and/or subsequent cascade overlap. However, a one-to-one correlation between the density of the observed amorphous domains and the ion dose could not be established.[21–23] Amorphization reached completion at much lower doses at the thin edges, where the HRTEM images were obtained (Fig. 5(D)), than in the thicker regions, where the SAED patterns were obtained (Fig. 4(D)), probably because of surface effects.[18,23] The D_c values were measured from the SAED observations.

The temperature dependencies of D_c (in dpa) for five X_2YO_4 phases—Mg_2SiO_4, α-Fe_2SiO_4, Mg_2GeO_4, Be_2SiO_4, and γ-$SiFe_2O_4$ under 1.5 MeV Kr^+ ion-beam irradiation—are plotted in Fig. 6. At 20 K, the D_c values for the five phases are similar (0.2–0.3 dpa); however, with increased temperature, the D_c value of each phase increased at different rates, resulting in very different temperatures above which the phase did not become amorphous.

During ion-beam irradiation, two competing processes, amorphization and relaxation/annealing, occur dynamically. Although the diffusion-driven recovery can be increased by irradiation-enhanced diffusion, this process is suppressed at low temperatures. Thus, an analysis of the temperature dependence of D_c, allows the two processes to be examined separately. Although, in general, D_c increases with increasing temperature, the slope of the D_c temperature curve is indicative of recovery rate. The rate of increase of D_c (highest to lowest) is, as shown in Fig. 6, Be_2SiO_4, Mg_2SiO_4, Mg_2GeO_4, α-Fe_2SiO_4, and γ-$SiFe_2O_4$. The differences in the change of recovery rate with temperature result in the differences in amorphization "resistance" at elevated temperatures. Thus, the order for the D_c rate of increase also can be regarded as a measure of the relative susceptibility of these materials to amorphization at elevated temperatures. The material's susceptibility or its rela-

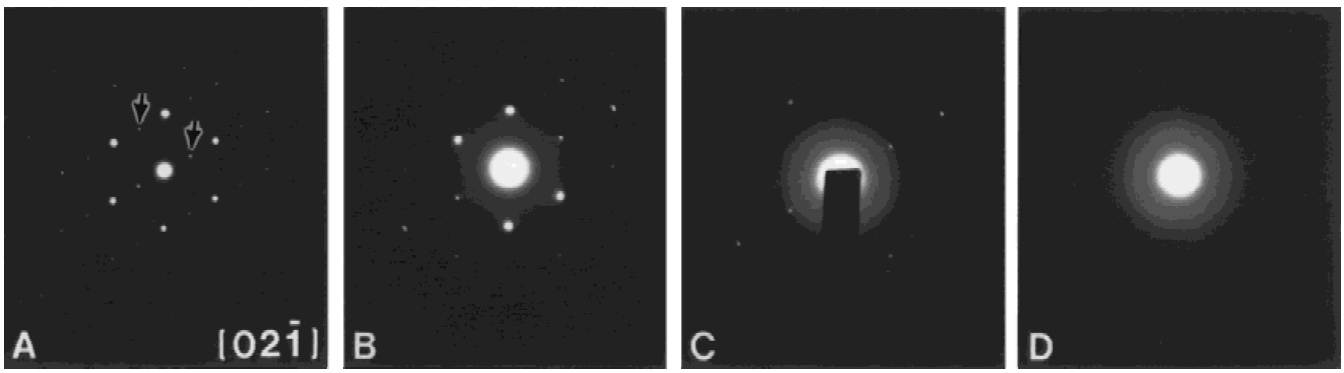

Fig. 4. Electron diffraction patterns of Mg_2SiO_4 obtained during *in situ* 1.5 MeV Kr^+-ion irradiation at 300 K to (A) 1.5×10^{18}, (B) 4.6×10^{18}, (C) 5.1×10^{18}, (D) 6.0×10^{18} ions/m^2.

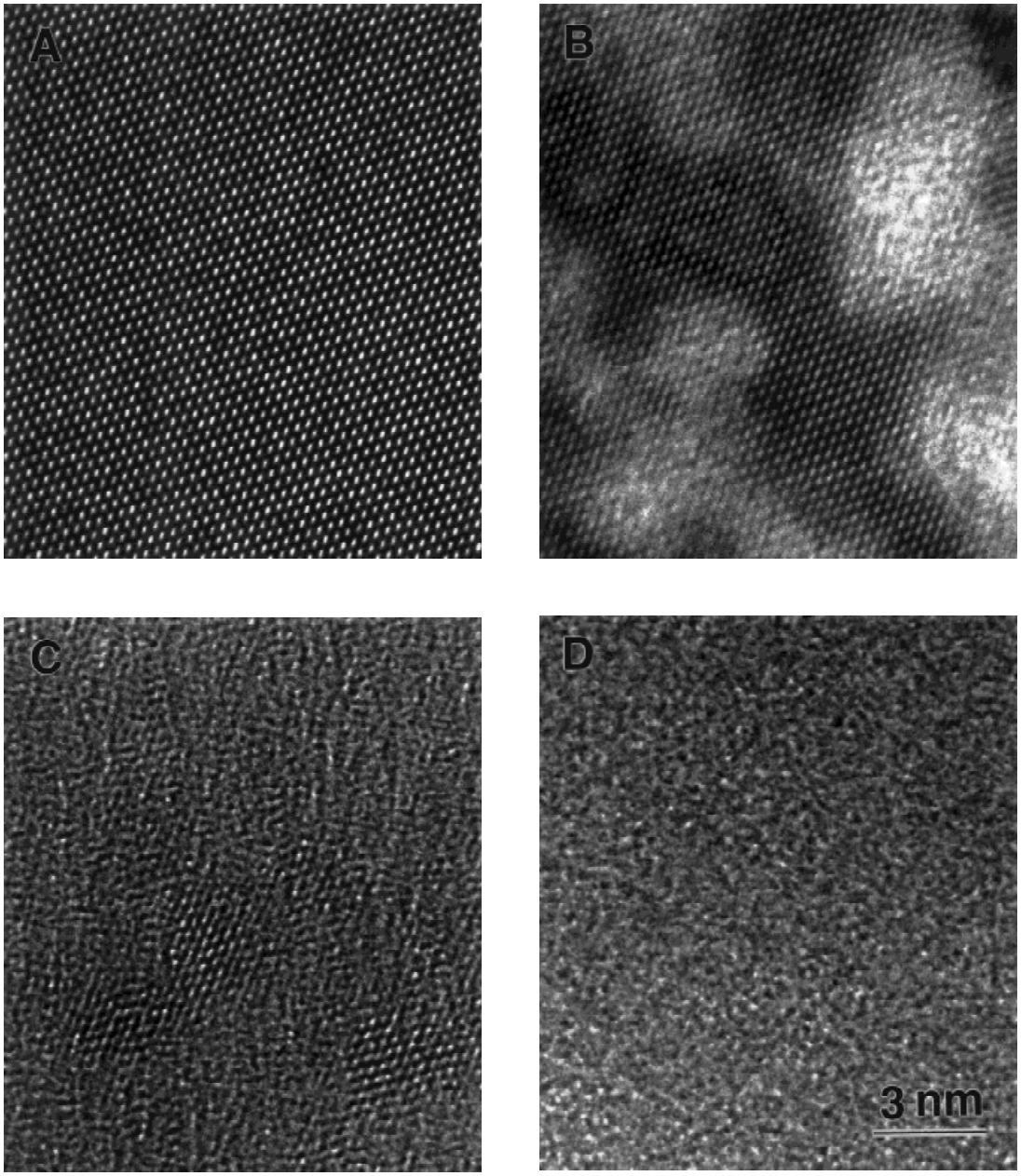

Fig. 5. HRTEM images from the thin edges of Mg_2SiO_4 taken (A) before and after 1.5 MeV Kr^+-ion-beam irradiations at room temperature to (B) 2.6×10^{16}, (C) 1.7×10^{17}, and (D) 1×10^{18} ions/m^2.

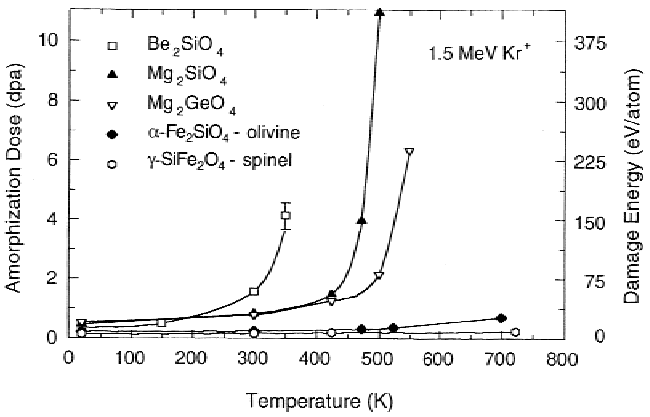

Fig. 6. Temperature dependence of critical amorphization dose of five X_2YO_4 phases under 1.5 MeV Kr^+ irradiation. Amorphization of $FeCr_2O_4$ spinel was achieved only after ~4 dpa at 20 K, but there was no evidence of amorphization in the $MgAl_2O_4$ spinel after a dose of 5.4 dpa at 20 K.

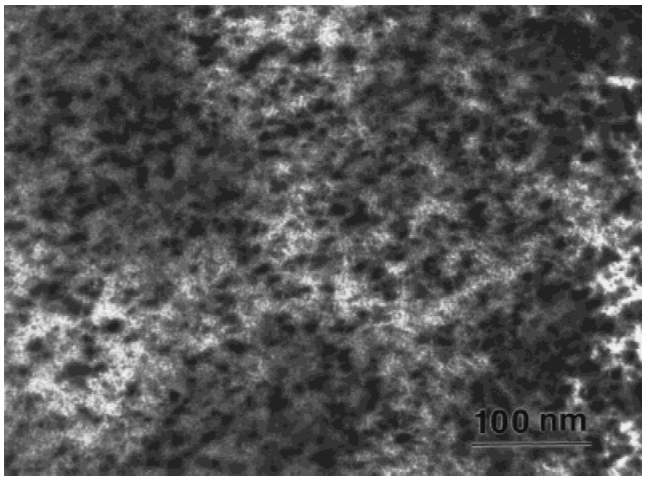

Fig. 7. Bright-field TEM micrograph ($g = 440$) showing the formation of small dislocation loops in $MgAl_2O_4$ after 1.5 MeV Kr^+ irradiation to 5.4 dpa at 20 K.

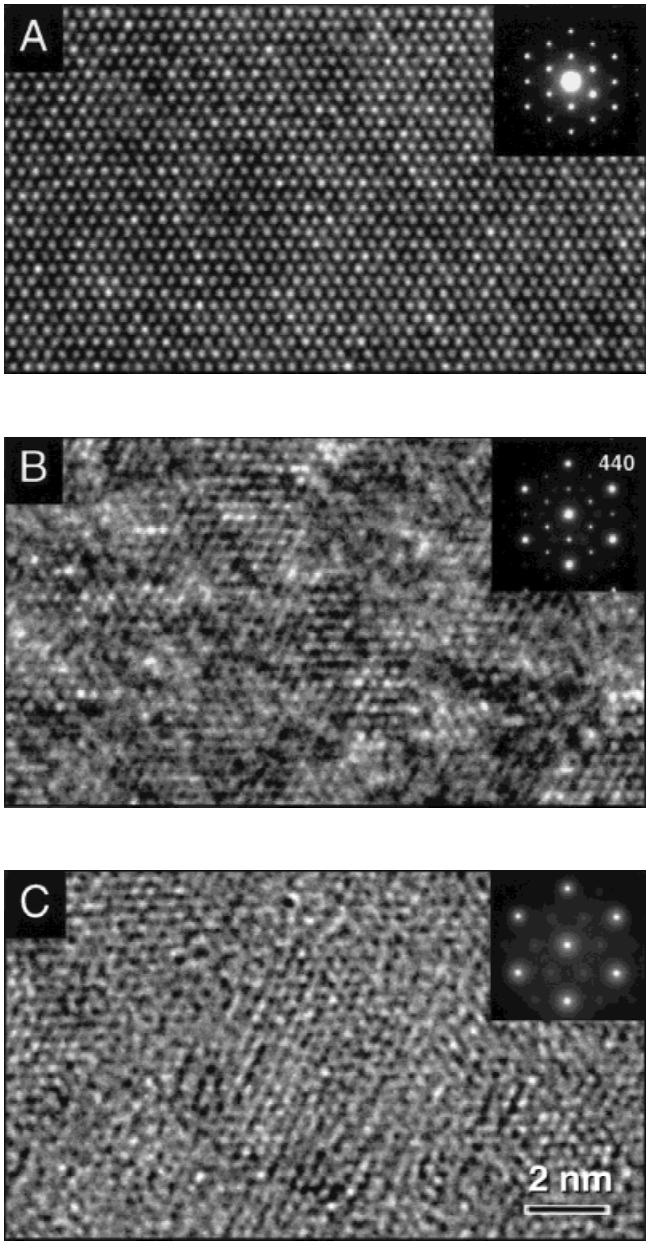

Fig. 8. HRTEM images and associated [111] zone SAED patterns of a $MgAl_2O_4$ sample irradiated with 1.5 MeV Kr^+ to 1×10^{20} ions/m^2 at 20 K (5.4 dpa in the beam center area) showing three distinct areas: (A) an undamaged area (outside the beam area), (B) a transition area from undamaged to damaged (at the edge of the ion beam), and (C) a fully damaged area (in the beam center).

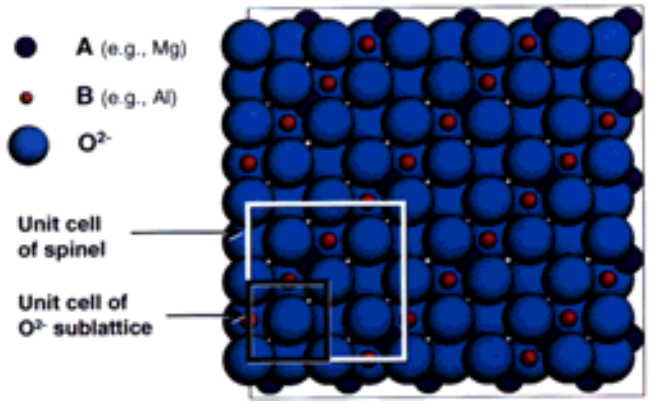

Fig. 9. Schematic (001) cross-section view of the spinel structure showing the relationship between the spinel unit cell and the unit cell of the oxygen sublattice. When cations disorder among all possible tetrahedral and octahedral sites, the unit cell of spinel reduces to that of the oxygen sublattice with a lattice parameter one-half of the original.

tive resistance to radiation-induced amorphization actually reflects the material's capability to recover the displacement damage caused by the irradiation. The D_c values determined for the three other compositions in the $(Mg,Fe)_2SiO_4$ solid-solution system at room temperature[24] show an increased resistance to amorphization for Mg-rich compositions, which is consistent with data shown in Fig. 6.

Because of the differences in the densities and displacement energies of the various phases, the per-ion energy loss and damage production in the electron-transparent sample thickness are different. Although TRIM calculations were performed to convert the critical ion fluences to dpa, this conversion may not be accurate, because a constant E_d of 25 eV is assumed for all five materials. If we assume that thermal annealing is completely suppressed at ~0 K, then the dpa level at which the materials with the same or similar structures become amorphous should be the same at that temperature. Thus, the data in Fig. 6 can be normalized (by shifting the D_c values at 20 K to the same level) to account for the differences in E_d. However, for the five materials plotted in Fig. 6, this normalization does not appear to be important, because this conversion does not change the relative order for "susceptibility" to amorphization at elevated temperatures.

Data for the two spinel phases, $MgAl_2O_4$ and $FeCr_2O_4$, are not included in Fig. 6, because $MgAl_2O_4$ is not amorphized at 20 K, even after a dose as high as 5.4 dpa, and $FeCr_2O_4$ is amorphized only at 20 K after 4 dpa, which is at least 10 times higher than that of the materials shown in Fig. 6.

The structure of magnesium aluminate spinel ($MgAl_2O_4$) was very stable under irradiation, as compared with other phases. At 20 K, no amorphization was detected in a sample irradiated to 1×10^{20} ions/m^2 (~5.4 dpa). As a basis for comparison, all of the X_2YO_4 ceramics with the olivine structure amorphized at doses of $<3 \times 10^{18}$ ions/m^2 (<0.3 dpa) under the same irradiation conditions. At room temperature, a high density of dislocation loops developed in the spinel after 2×10^{19} ions/m^2. After 1×10^{20} ions/m^2, the dislocation loop density was estimated to be $>1.25 \times 10^{22}$/m^3, and loops were <10 nm in diameter. A similar microstructure of dislocation loops was also observed after irradiation to 5.4 dpa at 20 K (Fig. 7), indicating that the point defects were mobile, even at very low temperatures. HRTEM images and SAED patterns in Fig. 8 confirmed the crystalline nature of the spinel after 5.4 dpa at 20 K. In the [111] zone axis SAED pattern, the intensity of the diffraction maxima from the {220} planes decreased gradually to extinction (see SAED inserts in Figs. 8(B) and (C)). This change in diffraction pattern indicated that the lattice parameter ($a_0 = 0.808$ nm) had been reduced by one-half to 0.404 nm, which was exactly the lattice parameter for the face-centered-cubic (fcc) oxygen sublattice (very close to the ideal ccp).

The unit cell of the spinel lattice consists of eight oxygen subunit cells in which eight of the 64 tetrahedral sites and 16 of the 32 octahedral sites are occupied by A and B cations, respectively. When cations disorder among all possible tetrahedral and octahedral sites, all of the cation sites are statistically occupied. This reduces the repeat distance for the unit cell to that of the oxygen sublattice, $a_0 = 0.404$ nm, as shown in Fig. 9. The observation of cation disordering in irradiated $MgAl_2O_4$ has been previously reported.[25,26] In this study, we also have found similar disordering in forsterite and chromite prior to amorphization by ion irradiation. This cation-site disordering is different from the chemical disordering that occurs in many intermetallic compounds (where one type of atom simply ex-

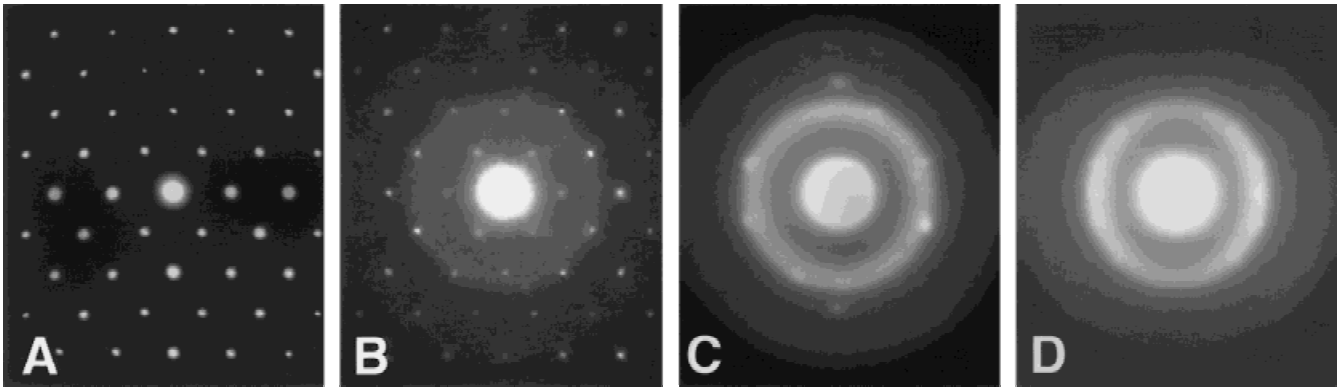

Fig. 10. SAED patterns of γ-$SiFe_2O_4$ taken before and after 1.5 MeV Kr^+ irradiation at 298 K: (A) original, and obtained after (B) 0.02, (C) 0.04, and (D) 0.06 dpa (the critical amorphization dose).

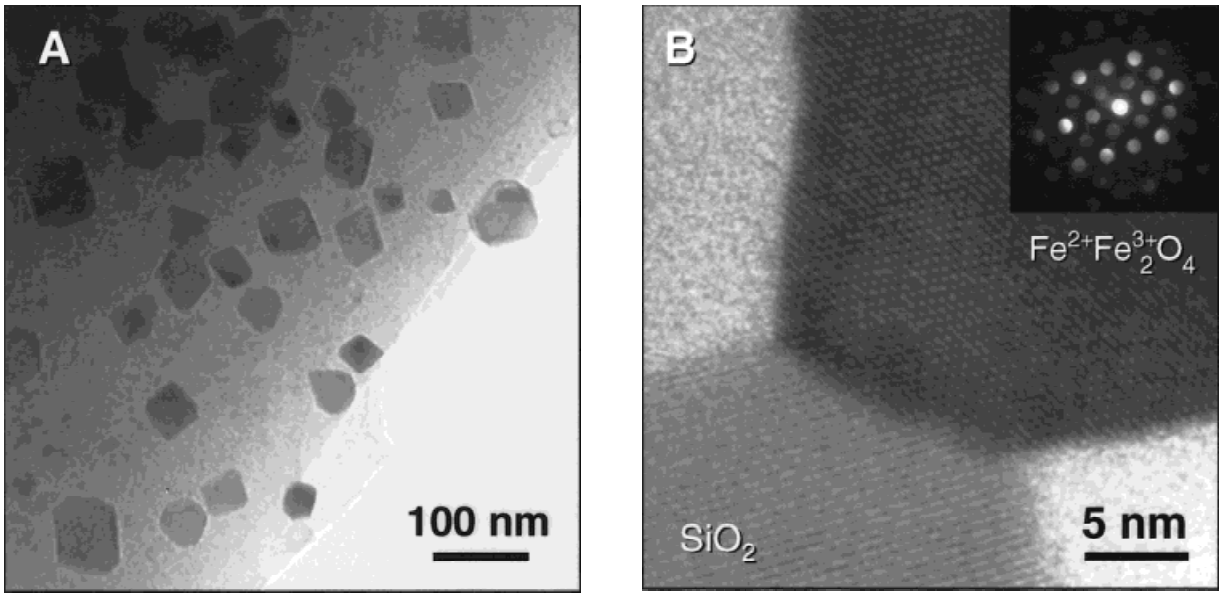

Fig. 11. TEM micrographs showing the microstructure of γ-$SiFe_2O_4$ spinel after 1.5 MeV Kr^+ irradiation to 2.9×10^{18} ions/m^2 at 873 K: (A) low-magnification bright-field image, (B) HRTEM image and a CBED pattern showing a magnetite and a quartz crystallite in an amorphous matrix. Identity of the crystallites was confirmed by nanobeam EDS analysis.

changes its position with another type of atom). The cation-site disordering in spinel can be considered as an interstitial vacancy recombination process. There are abundant vacancies in the structure that can serve as recombination centers, even before Frenkel pairs are created by collision events. From this structural perspective, it is possible to understand the low point-defect concentration or high recombination rate after fission–neutron irradiation of the spinel structure, as indicated by the thermal diffusivity measurement.[27] However, the resistance of spinel phases to radiation-induced amorphization cannot be attributed mainly to the presence of unoccupied octahedral and tetrahedral cation sites, because similar unoccupied sites are also present in the olivine structure-type that has been shown to be susceptible to radiation-induced amorphization. The cation-site disordering disturbs local charge balance, and the structure must adjust to restore charge balance, probably by incorporating point-defect complexes. This may eventually lead to amorphization at higher doses or lower temperatures because of point-to-point charge instabilities in the structure.

γ-$SiFe_2O_4$ was found to be very susceptible to irradiation-induced amorphization. At room temperature, an amorphous diffraction halo was apparent after an ion dose as low as 2.5×10^{17} ions/m^2 (0.02 dpa), and, after a dose of 8.5×10^{17} ions/m^2 (0.06 dpa), amorphization was complete (no diffraction maxima were present), as shown by the SAED patterns in Fig. 10. There was little change in the critical amorphization dose between 20 K (7.3×10^{17} ions/m^2) and 723 K (1.3×10^{18} ions/m^2). Thus, γ-$SiFeO_2O_4$ was even less radiation resistant than its olivine polymorph, fayalite (α-Fe_2SiO_4), which amorphized after 1.0×10^{18} ions/m^2 at 20 K and after 3.5×10^{18} ions/m^2 at 700 K. At 873 K, γ-$SiFe_2O_4$ continued to be amorphized. However, the amorphous phase recrystallized into magnetite ($Fe^{2+}Fe^{3+}_2O_4$), an inverse spinel, and quartz (SiO_2) under continued Kr^+ irradiation, as determined by convergent beam electron diffraction (CBED) and nanobeam energy dispersive X-ray spectroscopy (EDS) analysis.

Figure 11 shows the microstructure of γ-$SiFe_2O_4$ after irradiation to 2.89×10^{18} ions/m^2 at 873 K. The decomposition of γ-$SiFe_2O_4$ at the elevated temperatures is expected, because it is unlikely that the γ-$SiFe_2O_4$, a high-pressure metastable phase forms from the amorphous matrix during annealing. This result demonstrates that not all spinel structures are radiation resistant. However, because γ-$SiFe_2O_4$ is far outside of its pressure–temperature stability field, radiation-induced amorphization is enhanced by its thermodynamic instability.

$FeCr_2O_4$ demonstrated an intermediate resistance to radiation damage among the three spinels. Chromite became amorphous at 20 K after 6.0×10^{19} ions/m^2 (~4 dpa or >10 times

higher than that required to amorphize olivine structures at the same temperature). Figure 12 shows HRTEM micrograph and associated SAED patterns from the $FeCr_2O_4$ spinel (chromite) before and after 1.5 MeV Kr^+ irradiation. The cation disordering of the same type that occurred in $MgAl_2O_4$ at 20 K was observed in chromite prior to complete amorphization at 20 K and after 6.4 dpa at room temperature (Fig. 12(B)). However, no amorphization was detected at room temperature after the same dose.

IV. Discussion

Table I lists important material parameters that appear to be related to the susceptibility of the X_2YO_4 phases to radiation-induced amorphization. The phases are listed in the order of increasing amorphization resistance. The meaning of the parameters and their relationship to the relative amorphization resistance are discussed below.

ΔG_f is the standard free energy of formation from pure elements at 298 K. With the exception for Be_2SiO_4, the phase with the lower value of ΔG_f, or a phase more thermodynamically stable, is more resistant to amorphization at elevated temperatures.

The ionicity, calculated with Pauling's equation,[28] is an indication for the average bond-type. Within a given crystal structure-type, the composition with the higher ionicity is more resistant to amorphization at elevated temperatures. This agrees with the results compiled by Naquib and Kelly[28] for many simple oxides, as well as that of our previous study of five various ($(Mg,Fe)_2SiO_4$) olivine compositions irradiated at room temperature.[24] However, for different structure-types, the ionicity criterion is not very useful. For example, Mg_2SiO_4 (olivine structure-type) has an ionicity of 0.668, higher than that of the $MgAl_2O_4$ spinel (0.629), but the olivine is much more susceptible to radiation-induced amorphization than spinel. This suggests that the importance of bond-type may be secondary as compared with the importance of structure-type, although the recently developed structure-type criterion[29,30] based on a topological analysis does not predict the large difference in the susceptibility to amorphization between the olivine and spinel structure-types.

Average $\langle O–O \rangle$ distances can be used to evaluate the resistance to disruption between polyhedra in crystal structures. In general, resistance to amorphization increases with decreasing average $\langle O–O \rangle$ distance. However, because γ-$SiFe_2O_4$ is a high-pressure phase and is thermodynamically unstable, the small $\langle O–O \rangle$ distance is for a highly unstable configuration at low pressures. As noted by Zemann,[15] phenakite has the lowest interpolyhedral $\langle O–O \rangle$ distance among silicates (0.275 nm), and it has the highest resistance to amorphization at elevated temperatures among the silicates in this study. $MgAl_2O_4$ has a larger average $\langle O–O \rangle$ distance than Be_2SiO_4, but it exhibits higher resistance to amorphization, because it has the spinel structure-type.

The persistance of the oxygen sublattice of the spinel structure-type can be explained in terms of the near-perfect ccp arrangement of the oxygens in this structure. Figure 9 shows that most of the volume of the spinel unit cell is occupied by oxygen atoms, and the smaller cations occupy the tetrahedral and octahedral interstices. Elastic interactions during cascade formation cause disordering of the cations and displacements of oxygen anions, but minor relaxation can restore the oxygen-anion arrangement to the most efficient packing scheme (either ccp or hcp). Thus, the ordered sublattice of oxygen anions persists, while the cations remain disordered. In the case of spinel, the ccp arrangement is preferred, because this provides the widest spacing between interstices of similar coordination (e.g., reduces the possibility of Al^{3+} cations sharing adjacent octahedral sites). In contrast, the olivine structure-type has a highly distorted hcp arrangement of oxygen atoms that does not allow for the formation of the olivine structure as a result of relaxation to the hcp of the oxygen anions. The close packing of the oxygen sublattice, the abundant cation defect recombination centers, and the high point-defect mobility (indicated by the formation of dislocation loops at 20 K) all contribute to the resistance of the spinel structure-type to irradiation-induced amorphization.

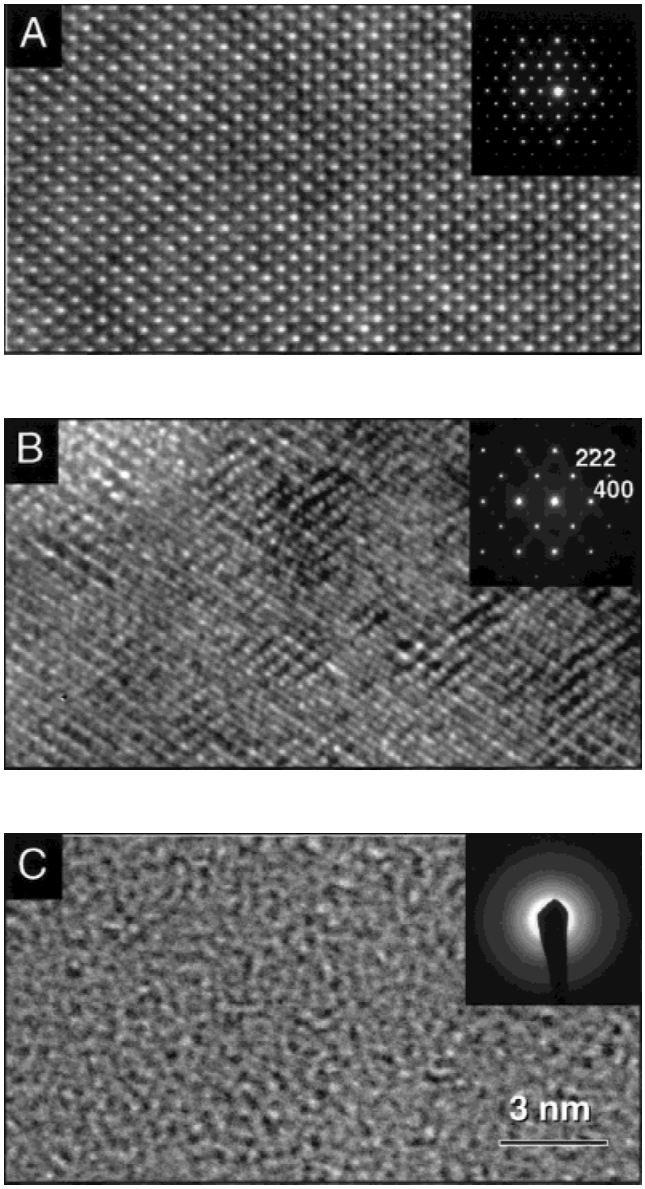

Fig. 12. HRTEM micrographs and associated SAED patterns from the $FeCr_2O_4$ spinel (chromite) before and after 1.5 MeV Kr^+ irradiation: (A) original, (B) 6.4 dpa at 300 K (cations are disordered as indicated by the disappearance of the 200 and 111 diffraction maxima), and (C) ~4 dpa at 20 K (structure is completely amorphized).

The average M–O bond compression coefficient, β, is a measure of the tolerance of the structure to elastic deformation. Within a structure-type, resistance to amorphization increases with decreasing β. The lowest β value among the listed phases is not phenakite. However, the crystal structure of phenakite consists only of BeO_4 and SiO_4 tetrahedra, whereas the crystal structures of spinel and olivine are comprised of BO_6 octahedra and AO_4 tetrahedra. Their structural configurations are very different. These data indicate again that the structure-type is more important in estimating amorphization resistance.

d_X/d_Y is the ratio between octahedral M–O and tetrahedral M–O distances. This parameter has been used to indicate the relative stability of spinel or olivine structural-types. For instance, if $d_X/d_Y < 1.19$, then the spinel structure is stable; otherwise, the olivine structure is stable, at normal pressure.[31]

Table I. Selected Material Parameters of the X_2YO_4 Phases Included in This Study†

Phase	ΔG_f	Ionicity	<O–O> (nm)	β ($Mbar^{-1}$)	d_X/d_Y	Φ	*F*
γ-$SiFe_2O_4$ (spinel)		0.504	0.2965		1.294	0.383	
α-Fe_2SiO_4 (olivine)	−1379.4	0.504	0.3049	146	1.324	0.383	0.147
Mg_2GeO_4 (olivine)		0.658		138			0.127
Mg_2SiO_4 (olivine)	−2051.3	0.668	0.2944	135	1.294	0.295	0.145
Be_2SiO_4 (phenakite)	−2033.7	0.554	0.2750	66		0.177	0.190
$FeCr_2O_4$ (spinel)		0.574		107		0.292	0.072
$MgAl_2O_4$ (spinel)	−2174.9	0.629	0.2792	96	1.001	0.198	0.067

†Phases are listed in the order of increasing resistance to ion-beam-induced amorphization. See text for detailed discussion on the meaning of the parameters.

d_X/d_Y for γ-$SiFe_2O_4$ is 1.294 (>1.19). Thus, topologically, this high-pressure phase is not stable and is less resistant to radiation-induced amorphization although it has the spinel structure-type. Therefore, we cannot conclude that composition is more important than the structure-type in determining the amorphization resistance, based on the very similar amorphization doses between α-Fe_2SiO_4 and γ-$SiFe_2O_4$.

The structural deviation parameter, Φ, is defined as[32]

$$\Phi = 2|r_{oct}/r_{O^{2-}} - 0.414| + |r_{tet}/r_{O^{2-}} - 0.255| \quad (1)$$

where r_{oct} is the ionic radius of the octahedral cation, r_{tet} the ionic radius of the tetrahedral cation, and $r_{O^{2-}}$ the ionic radius of O^{2-}. Φ indicates the deviation from perfect octahedral and tetrahedral close packing in a structure. Apparently, any distortion from the perfect atomic packing contributes to the relative instability of the structure. For an ideal spinel or olivine structure, $\Phi = 0$ where all the oxygen atoms touch each other, forming an ideal close-packing arrangement. With the exception of Be_2SiO_4, which does not have octahedral sites, the resistance to amorphization indeed increases with decreasing Φ. $MgAl_2O_4$ spinel has the highest resistance to radiation-induced amorphization, because it has the smallest deviation from ideal close packing of the oxygen sublattice.

F is the average field strength of bonds and is introduced as a simple parameter to describe the tendency of glass formation in oxides:[33]

$$F = \frac{z_1 z_2 e}{a^2} \quad (2)$$

where *z* is the charge on the ion, *e* the electron charge, and *a* the distance between ions 1 and 2. *F* is an indication of the bond strength. Because atomic rearrangement during crystallization involves the breaking and reforming of bonds, Sun[34] has attributed the higher glass-forming ability of an oxide to the stronger bonding in the structure. Through analyses of a group of oxides in the $MgO–Al_2O_3–SiO_2$ system, it has been found that good glass formers are also susceptible to radiation-induced amorphization and that this can be understood based on a cascade–quenching model.[35] To apply Eq. (2) to complex crystalline phases, the effective charge (electrostatic charge divided by coordination number) instead of *z* is used.[35] Except for the anomaly of phenakite, *F* provides a good correlation to the susceptibility to amorphization, as shown in Table I.

The above analysis also can be applied to other solid-state amorphization processes. For example, the pressure required to completely amorphize various (Fe,Mg)-olivine compositions also increases with the increasing Mg content in pressure-induced amorphization, from ~35–40 GPa for fayalite to ~70 GPa for forsterite.[36] The $MgAl_2O_4$ spinel is not amorphized at pressures <100 GPa.[37] Amorphization under high pressures has been considered as essentially pressure-induced melting,[38] and, in this perspective, it has a great similarity to radiation-induced amorphization.[39]

The slope of the D_c temperature curves in Fig. 6 is also a function of the density of the material. The lower the sample density, the faster the curve rises (resulting in a lower activation energy for recovery and lower critical amorphization temperature). The effect of the lower sample density is similar to the effect of the smaller projectile mass on the amorphization dose,[40] although they are not of the same magnitude. This dependence and similarity can be qualitatively explained in terms of the size and/or density of the collision cascades, or the amorphization efficiency in the target. For a given target, the cross section for nuclear collision is larger when a large projectile mass is used, thus creating a larger displacement cascade or more atomic displacements in the thin TEM specimen. The same relation is true for a given projectile mass in a target of higher density. Reference 41 shows that the per-ion vacancy production in a 200 nm thick foil varies from 2200 for Be_2SiO_4 (2.96 g/cm^3) to 3500 for Fe_2SiO_4 (4.392 g/cm^3). The greater the per-ion vacancy production, the larger or denser the displacement cascades. Because the activation energies for the dynamic recovery of these X_2YO_4 phases calculated using a model described by Weber *et al.*[20] are too low (<0.1 eV) for crystal nucleation (usually several eV), it is assumed that the recovery in the amorphous cascade region is mainly through the epitaxial regrowth of the surrounding crystalline volume.[23,35] The recovery rate for a smaller cascade (which may result in a smaller amorphous domain) is faster than that of a larger cascade, because the surface-area to volume ratio is larger for the smaller cascade, thus allowing more-efficient epitaxial recrystallization (i.e., reduction of the amorphous volume).

V. Conclusions

Through comparison of the temperature dependence of amorphization dose for seven X_2YO_4 phases, we have found that the structure-type, the chemical composition (which affects bond-type and bond strength within a given structure-type), and the thermodynamic stability are important in determining the susceptibility of a material to radiation-induced amorphization. Olivines are generally more susceptible to radiation-induced amorphization than the spinels. However, the unstable high-pressure spinel (γ-$SiFe_2O_4$) is more easily amorphized than its olivine counterpart fayalite (α-Fe_2SiO_4) at all temperatures. The resistance of spinel phases to radiation-induced amorphization is not mainly due to the unfilled octahedral and tetrahedral cation sites (because similar empty sites are also available in the olivine structure) but rather is related to the cubic-closest-packing of the oxygen sublattice and the associated high point-defect mobility. The susceptibility to amorphization of a spinel phase increases with increasing deviation of oxygen sublattice from the ideal close-packing arrangement of the anions.

Acknowledgments: The authors are grateful to Dr. H. R. Westrich (Sandia National Laboratories) and Dr. H. W. Green II (University of California-Riverside) for providing the synthetic samples of the silicate and germanate olivines, respectively, and to Dr. Y. Fei (Geophysical Laboratory, Carnegie Institution, Washington, D.C.) for providing the γ-$SiFe_2O_4$ specimen. We also thank the HVEM-Tandem Facility staff, Argonne National Laboratory, i.e., L. L. Funk, E. A. Ryan, and S. T. Ockers, for assistance during ion irradiation and *in situ* TEM. The high-resolution electron microscopy was completed at the

Electron Microbeam Analysis Facility of the Department of Earth and Planetary Sciences, University of New Mexico.

References

[1]L. W. Hobbs, F. W. Clinard Jr., S. J. Zinkle, and R. C. Ewing, "Radiation Effects in Ceramics," *J. Nucl. Mater.*, **216**, 291–321 (1994).

[2]K. E. Sickafus, A. G. Larson, N. Yu, M. Nastasi, G. W. Hollenberg, F. A. Garner, and R. C. Bradt, "Cation Disordering in High-Dose Neutron-Irradiated Spinel," *J. Nucl. Mater.*, **219**, 128–34 (1995).

[3]N. Yu, K. E. Sickafus, and M. Nastasi, "First Observation of Amorphization in Single-Crystal $MgAl_2O_4$ Spinel," *Philos. Mag. Lett.*, **70**, 235–40 (1994).

[4]G. P. Pells, "Radiation-Induced Electrical Conductivity in $MgAl_2O_4$ Spinel," *J. Nucl. Mater.*, **184**, 183–90 (1991).

[5]R. Yamada, S. J. Zinkle, and G. P. Pells, "Microstructure of Al_2O_3 and $MgAl_2O_4$ Preimplanted with H, He, C, and Irradiated with Ar^+ Ions," *J. Nucl. Mater.*, **290**, 191–203 (1994).

[6]A. Ibarra, R. Vila, and F. A. Garner, "Optical and Dielectric Properties of Neutron-Irradiated $MgAl_2O_4$ Spinels," *J. Nucl. Mater.*, **237**, 1336–39 (1996).

[7]S. J. Zinkle and G. P. Pells, "Microstructure of Al_2O_3 and $MgAl_2O_4$ Irradiated at Low Temperatures," *J. Nucl. Mater.*, **253**, 120–32 (1998).

[8]D. C. Rubie and A. J. Brearley, "Phase Transitions Between β- and γ-$(Mg,Fe)_2SiO_4$ in the Earth's Mantle: Mechanisms and Rheological Implications," *Science* (*Washington, D.C.*), **264**, 1445–48 (1994).

[9]M. B. Kruger, J. H. Nguyen, W. Caldwell, and R. Jeanloz, "Equation of State of $MgAl_2O_4$ Spinel to 65 GPA," *Phys. Rev. B: Condens. Matter*, **56**, 1–4 (1997).

[10]T. Yagi, M. Akaogi, O. Shimomura, T. Suzuki, and S. Akimoto, "*In Situ* Observation of the Olivine–Spinel Phase Transformation in Fe_2SiO_4 Using Synchchrotron Radiation," *J. Geophys. Res.*, **92**, 6207–13 (1987).

[11]M. Akaogi, E. Ito, and A. Navrotsky, "Olivine-Modified Spinel–Spinel Transitions in the System Mg_2SiO_4–Fe_2SiO_4: Calorimetric Measurements, Thermochemical Calculation, and Geophysical Application," *J. Geophys. Res.*, **94**, 15671–85 (1989).

[12]A. J. Brearly, D. C. Rubie, and E. Ito, "Mechanisms of the Transformations Between the α, β, and γ Polymorphs of Mg_2SiO_4 at 15 GPa," *Phys. Chem. Miner.*, **18**, 343–58 (1992).

[13]N. L. Ross and A. Navrotsky, "The Mg_2SiO_4 Olivine–Spinel Transition," *Phys. Chem. Miner.*, **14**, 473–81 (1987).

[14]M. D. Jackson and R. G. Gordon, "A MEG Study of the Olivine and Spinel Forms of Mg_2SiO_4," *Phys. Chem. Miner.*, **15**, 514–20 (1988).

[15]J. Zemann, "The Shortest Known Interpolyhedral O–O Distance in a Silicate," *Z. Kristallogr.*, **175**, 299–303 (1986).

[16]C. W. Allen, L. L. Funk, E. A. Ryan, and S. T. Ockers, "*In Situ* Ion Irradiation Implantation Studies in the HVEM-Tandem Facility at Argonne National Laboratory," *Nucl. Instr. Meth. B*, **40–41**, 553–56 (1989).

[17]J. F. Ziegler, J. P. Biersack, and U. Littmark, *The Stopping and Range of Ions in Solids.* Pergamon, New York, 1985.

[18]L. M. Wang, "Applications of Advanced Electron Microscopy Techniques to the Studies of Radiation Effects in Ceramic Materials," *Nucl. Instr. Meth. B*, **141**, 312–25 (1998).

[19]R. C. Ewing and T. J. Headley, "Alpha-recoil Damage in Natural Zirconolite ($CaZrTi_2O_7$)," *J. Nucl. Mater.*, **119**, 102–109 (1983).

[20]W. J. Weber, R. C. Ewing, and L. M. Wang, "The Radiation-Induced Crystalline to Amorphous Transition in Zircon," *J. Mater. Res.*, **9**, 688–98 (1994).

[21]M. L. Miller and R. C. Ewing, "Image Simulation of Partially Amorphous Materials," *Ultramicroscopy*, **48**, 203–37 (1992).

[22]L. M. Wang, M. L. Miller, and R. C. Ewing, "HRTEM Study of Displacement Cascade Damage in Krypton-Ion-Irradiated Silicate–Olivine," *Ultramicroscopy*, **51**, 339–47 (1993).

[23]L. M. Wang and W. J. Weber, "Transmission Electron Microscopy Study of Ion-Beam-Induced Amorphization of $Ca_2La_8(SiO_4)_6O_2$," *Philos. Mag. A*, **79**, 237–53 (1999).

[24]L. M. Wang and R. C. Ewing, "Ion-Beam-Induced Amorphization of Complex Ceramic Materials—Minerals," *MRS Bull.*, **17** [5] 38–44 (1992).

[25]K. E. Sickafus, A. C. Larson, N. Yu, M. Nastasi, G. W. Hollenberg, F. A. Garner, and R. C. Bradt, "Cation Disorder in High-Dose, Neutron-Irradiated Spinel," *J. Nucl. Mater.*, **219**, 128–34 (1995).

[26]N. Bordes, L. M. Wang, R. C. Ewing, and K. E. Sickafus, "Ion-Beam-Induced Disordering and Onset of Amorphization in Spinel by Defect Accumulation," *J. Mater. Res.*, **10**, 981–85 (1995).

[27]F. W. Clinard Jr. and L. W. Hobbs, "Radiation Effects in Non-Metals"; pp. 387–471 in *Physics of Radiation Effects in Crystals.* Edited by R. A. Johnson and A. N. Orlov. Elsevier, Amsterdam, The Netherlands, 1986.

[28]H. M. Naquib and R. Kelly, "Criteria for Bombardment-Induced Structural Changes in Non-Metallic Solids," *Radiat. Eff.*, **25**, 1–12 (1975).

[29]L. W. Hobbs, A. N. Sreeram, C. E. Jesurum, and B. A. Berger, "Structural Freedom, Topological Disorder, and the Irradiation-Induced Amorphization of Ceramic Structures," *Nucl. Instr. Meth. B*, **116**, 18–25 (1996).

[30]L. W. Hobbs, C. E. Jesurum, V. Pulim, and B. Berger, "Topological Modeling of Cascade Amorphization in Network Structures Using Local Rules," *Mater. Sci. Eng.* A, **253**, 16–29 (1998).

[31]R. M. Hazen and A. T. Prewitt, "Effects of Temperature and Pressure on Interatomic Distances in Oxygen-Based Minerals," *Am. Miner.*, **62**, 309–15 (1977).

[32]L. M. Wang, W. L. Gong, N. Bordes, R. C. Ewing, and Y. Fei, "Effects of Ion Dose and Irradiation Temperature on the Microstructure of Three Spinel Compositions," *Mater. Res. Soc. Symp. Proc.*, **373**, 407–12 (1995).

[33]H. Scholze, *Glass—Nature, Structure, and Properties*; p. 107. Springer-Verlag, New York, 1991.

[34]K. H. Sun, "Fundamental Condition of Glass Formation," *J. Am. Ceram. Soc.*, **30**, 277 (1947).

[35]S. X. Wang, L. M. Wang, R. C. Ewing, and R. H. Doremus, "Ion-Beam-Induced Amorphization in MgO–Al_2O_3–SiO_2. Part II: Empirical Model," *J. Non-Cryst. Solids*, 214–24 (1998).

[36]F. Guyot and B. Reynard, "Pressure-Induced Structural Modifications and Amorphization in Olivine Compounds," *Chem. Geol.*, **96**, 411–20 (1992).

[37]P. Richet and P. Gillet, "Pressure-Induced Amorphization of Minerals: A Review," *Eur. J. Miner.*, **9**, 907–33 (1997).

[38]S. M. Sharma and S. K. Sikka, "Pressure-Induced Amorphization of Materials," *Prog. Mater. Sci.*, **40** [1] 1–77 (1996).

[39]N. Q. Lam and P. R. Okamoto, "A Unified Approach to Solid-State Amorphization and Melting," *MRS Bull.*, **19** [7] 41–46 (1994).

[40]J. Koike, P. R. Okamoto, and L. E. Rehn, "The Dose, Temperature, and Projectile-Mass Dependence for Irradiation-Induced Amorphization of CuTi," *J. Mater. Res.*, **4**, 1143–50 (1989).

[41]L. M. Wang, W. L. Gong, and R. C. Ewing, "Amorphization and Dynamic Recovery of A_2BO_4 Structure Types during 1.5 MeV Krypton-Ion-Beam Irradiations," *Mater. Res. Soc. Symp. Proc.*, **316**, 247–52 (1994). □